Thermodynamic nonequilibrium effects in bubble coalescence: A discrete Boltzmann study

Guanglan Sun,[1,2] Yanbiao Gan ,[2] Aiguo Xu ,[3,4,5,*] Yudong Zhang ,[6] and Qingfan Shi[1,†]

[1]*School of Physics, Beijing Institute of Technology, Beijing 100081, China*
[2]*Hebei Key Laboratory of Trans-Media Aerial Underwater Vehicle, School of Liberal Arts and Sciences,*
North China Institute of Aerospace Engineering, Langfang 065000, China
[3]*National Key Laboratory of Computational Physics, Institute of Applied Physics and Computational Mathematics,*
P.O. Box 8009-26, Beijing 100088, China
[4]*State Key Laboratory of Explosion Science and Technology, Beijing Institute of Technology, Beijing 100081, China*
[5]*HEDPS, Center for Applied Physics and Technology, and College of Engineering, Peking University, Beijing 100871, China*
[6]*School of Mechanics and Safety Engineering, Zhengzhou University, Zhengzhou 450001, China*

The thermodynamic nonequilibrium (TNE) effects in a coalescence process of two initially static bubbles under thermal conditions are investigated by a discrete Boltzmann model. The spatial distributions of the typical nonequilibrium quantity, i.e., nonorganized momentum fluxes (NOMFs), during evolutions are investigated in detail. The density-weighted statistical method is used to highlight the relationship between the TNE effects and the morphological and kinetics characteristics of bubble coalescence. The results show that the *xx* component and *yy* component of NOMFs are antisymmetrical; the *xy* component changes from an antisymmetric internal and external double quadrupole structure to an outer octupole structure during the coalescence process. Moreover, the evolution of the averaged *xx* component of NOMFs provides two characteristic instants, which divide the nonequilibrium process into three stages. The first instant, when the averaged *xx* component of the NOMFs reaches its first local minimum, corresponds to the moment when the mean coalescence speed gets the maximum, and at this time the ratio of minor and major axes is about $1/2$. The second instant, when the averaged *xx* component of the NOMFs gets its second local maximum, corresponds to the moment when the ratio of minor and major axes becomes 1 for the first time. It is interesting to find that the three quantities, TNE intensity, acceleration of coalescence, and the slope of boundary length, show a high degree of correlation and attain their maxima simultaneously. The surface tension and the heat conduction accelerate the process of bubble coalescence, while the viscosity delays it. Both the surface tension and the viscosity enhance the global nonequilibrium intensity, whereas the heat conduction restrains it. These TNE features and findings present some insights into the kinetics of bubble coalescence.

I. INTRODUCTION

Bubble coalescence is frequently encountered in many applications such as two-phase electrochemical systems [1–3], biological and pharmaceutical applications [4–7], and boiling water-cooled packed bed reactors [8–10]. In some cases, the coalescence of bubbles needs to be prevented, while in other cases, it must be promoted. Therefore, it is necessary to fundamentally understand the essence of bubble coalescence, including its basic dynamics phenomena and morphological characteristics, particularly the commonly neglected nonequilibrium effects and behaviors of the system.

There have been many studies on the phenomenon and mechanism of bubble coalescence through experiments [11–31], theoretical analyses [12,32,33], and numerical simulations [14,34–44]. Common experimental research methods include observing bubble swarms under various conditions

[20–22,31], using the bubbles growing from capillaries and putting them side by side [13,16,17], using the underwater electric discharge method [14,23,24], and studying the dynamic changing process of a thin liquid film and measuring the nonequilibrium forces between two air phases by atomic force microscopy [25–29] and interferometry [27,28,30]. Specifically, Vakarelski *et al.* [25] experimentally studied microbubbles around 100 μm in size by using an atomic force microscope. They directly measured the nonequilibrium force between two bubbles in water under controlled collision. Their experimental results together with detailed modeling demonstrated that the coupling of hydrodynamic flow, attractive van der Waals–Lifshitz forces, and bubble deformation plays a very important role during the coalescence process. They revealed the physical essence of boundary conditions at the air-water interface and mechanisms leading to bubble coalescence. Liu *et al.* [30] investigated the rapid thinning of a liquid film between two quickly colliding bubbles using high-speed interferometry. They found that the Marangoni stress can balance the shear stress and prevents the thinning of the liquid film at a small film thickness. There is

---

*Corresponding author: Xu_Aiguo@iapcm.ac.cn
†Corresponding author: qfshi123@bit.edu.cn

dynamic competition between various stresses. Once they reach equilibrium, the interface becomes immobile. Stover *et al.* [14] first investigated the oscillating characteristics of the coalescence of bubbles with different sizes, viscosities, and surface tensions. They found that surface waves, starting at the onset of coalescence, were superimposed on the motion of the bubbles. These waves are likely to enhance the mass transfer efficiency but have little effect on the overall dynamics. Then they simulated the dynamics of coalescence by solving the nonlinear Navier-Stokes equations, and their results were partly consistent with the experiments due to the failure to reflect the actual initial state. The approximate analytic solution of the neck radius $r_n \sim Bt^{1/2}$ was given in Refs. [12,32,33,40]; the prefactor B was positively correlated with the surface tension coefficient and negatively correlated with the viscosity coefficient. Zheng *et al.* developed a free-energy lattice Boltzmann method (LBM) to trace the bubble coalescence at a high density ratio [36]. In their LBM, the interface is naturally captured, and the Cahn-Hilliard equation can be recovered without any additional terms [35,36]. Chen *et al.* studied the coalescence of unequal-size and equal-size bubbles [37–39,41] by developing an LBM to solve the Navier-Stokes equations and Cahn-Hilliard equation. Power-law relations between the global coalescence time and size inequality and the effects of the Ohnesorge number (Oh) on those power-law relations have been clarified [37–39]. They further demonstrated that unequal bubbles coalesce faster than equal bubbles and clarified the relations between characteristic coefficients and Oh [39].

As mentioned above, the nonequilibrium forces between two bubbles in the process of fluid film thinning, the slow variables (density, temperature, pressure, the surface tension, etc.), and the morphological characteristics during bubble coalescence have been widely investigated by experimental, theoretical, and numerical simulation methods from various perspectives. Despite the significant progress to date, the thermodynamic nonequilibrium (TNE) effects during the whole process of bubble coalescence are rarely taken into consideration, especially in experimental research due to the inconvenience of the technical measurement. However, as we will show in this paper, TNE behaviors are of great importance for this dynamic and complex process because there are stronger TNE effects from the onset of coalescence to the formation of the first unsteady circular bubble, and the TNE effects significantly influence the morphological characteristic and determine the coalescence speed, macroscopic quantities, phase transformation rate, etc. A careful study of these behaviors is beyond the physical capability of the traditional hydrodynamic model. In this work, we resort to the recently developed discrete Boltzmann method (or model; DBM).

The DBM [45–52] is a mesoscopic kinetic model. In 2012, Xu *et al.* [45] pointed out that, under the framework of the LBM and under the condition that does not use the nonphysical Boltzmann equation and kinetic moments, the nonconservative moments of $(f_i - f_i^{eq})$ can be used to describe how and how much the system deviates from the thermodynamic equilibrium and to check the corresponding effects due to the deviation from the thermodynamic equilibrium. This was the starting point of the current DBM study.

In 2015, Xu *et al.* [46] proposed opening a phase space using the nonconservative moments of $(f_i - f_i^{eq})$ and described the extent of TNE using the distance between a state point to the origin in the phase space or its subspace. In 2018, Xu *et al.* [47] further developed the nonconservative moment phase space description methodology. They proposed using the distance D between two state points to roughly describe the difference between two states deviating from their thermodynamic equilibria, and the reciprocal of the distance $1/D$ is defined as a similarity of deviating from thermodynamic equilibrium. The mean distance during a time interval of D, $\bar{D}$, is used to roughly describe the difference between the two corresponding kinetic processes, and the reciprocal of $\bar{D}$, $1/\bar{D}$, is defined as a process similarity. In 2021, Xu *et al.* [52] extended the phase space description methodology to any set of system characteristics. They used a set of (independent) characteristic quantities to open phase space and used this space and its subspaces to describe the system properties. A point in the phase space corresponds to a set of characteristic behaviors of the system. Distance concepts in a phase space or its subspaces are used to describe the difference and similarity of behaviors. To date, the DBM has been used in various multiphase flow systems, such as hydrodynamic instabilities [49,53–57], compressible flows under impact [48–51], nonequilibrium combustion [58–60], nonequilibrium phase separation [61–65], and droplet collision [66]. For example, Gan *et al.* [61] used a DBM to study the hydrodynamic nonequilibrium and TNE effects in the phase separation process. They defined TNE strength and discovered that the time evolution of the TNE intensity provides a convenient and efficient physical criterion to discriminate the stages of spinodal decomposition and domain growth. Lai *et al.* [55] studied the effects of compressibility on Rayleigh-Taylor instability (RTI) by the DBM. They found that the local TNE can be used to track the interfaces and discriminate between the two stages of the RTI effectively. Zhang *et al.* [66] researched droplet collisions using the DBM on the basis of a discrete Enskog equation. They found that the mean strength of the nonorganized momentum fluxes (NOMFs) $\bar{D}_2^*$ was always prominently greater than that of $\bar{D}_3^*$, and $\bar{D}_2^*$ can be used to identify the different stages of the collision process and to recognize different types of collisions. Zhang *et al.* [62] analyzed entropy production associated with the TNE of the thermal phase separation. They found that NOMFs and the nonorganized energy fluxes (NOEFs) both directly contribute to entropy production.

Compared with previous studies of phase separation [61–65], in the bubble coalescence system, the spatial distributions of nonequilibrium behaviors are axisymmetric, and the strengths of nonequilibrium effects are relatively strong. In addition to the statistical properties, the spatiotemporal evolution characteristics of NOMFs and the relations between the thermodynamic nonequilibrium behaviors and the morphological and kinematic characteristics describing bubble coalescence are analyzed in detail via a compressible multiphase DBM. The physical model is presented in Sec. II; simulations and an analysis of the nonequilibrium characteristics during bubble coalescence and the effects of the surface tension, viscosity, and heat conduction are presented in Sec. III. The conclusions are made in Sec. IV.

II. CONSTRUCTION OF THE DBM

According to molecular kinetic theory, the evolution equation of the molecular velocity distribution function reads

$$\frac{\partial f}{\partial t} + \mathbf{v} \cdot \frac{\partial f}{\partial \mathbf{r}} + \mathbf{a} \cdot \frac{\partial f}{\partial \mathbf{v}} = \left(\frac{\partial f}{\partial t}\right)_c, \tag{1}$$

where $f = f(\mathbf{r}, \mathbf{v}, t)$ is the molecular velocity distribution function and $\mathbf{r}$, $\mathbf{v}$, and $\mathbf{a}$ are the position space coordinate, the velocity space coordinate, and the acceleration generated by the total extra force, respectively. $(\partial f/\partial t)_c$ represents the collision term. If the constraint $\int \boldsymbol{\Psi}(\partial f/\partial t)_c d\mathbf{v} = \int -\boldsymbol{\Psi}(f - f^{eq})/\tau d\mathbf{v}$ is satisfied, the collision term can be linearized, $(\partial f/\partial t)_c = -(f - f^{eq})/\tau$ [67], where $\boldsymbol{\Psi} = [1, \mathbf{v}, \mathbf{vv}, \mathbf{vvv}]^T$, τ is the relaxation time, and $f^{eq} = \rho(1/2\pi T)^{D/2} \exp[-(\mathbf{v} - \mathbf{u})^2/2T]$ is the Maxwellian distribution function in the Bhatnagar-Gross-Krook (BGK) model. D is the spatial dimension, and $D = 2$ in this paper.

To describe the nonideal gas effects, Gonnella, Lamura, and Sofonea (GLS) improved the Watari-Tsutahara model [68] by introducing an appropriate force term on the right-hand side of the Boltzmann-BGK equation. Then the GLS-Boltzmann equation is extended as

$$\frac{\partial f}{\partial t} + \mathbf{v} \cdot \frac{\partial f}{\partial \mathbf{r}} = -\frac{1}{\tau}(f - f^{eq}) + I, \tag{2}$$

with

$$I = -[A + \mathbf{B} \cdot (\mathbf{v} - \mathbf{u}) + (C + C_q)(\mathbf{v} - \mathbf{u})^2]f^{eq}. \tag{3}$$

Here,

$$A = -2(C + C_q)T, \tag{4}$$

$$\mathbf{B} = \frac{1}{\rho T} \boldsymbol{\nabla} \cdot \left[(P^{CS} - \rho T)\mathbf{I} + \boldsymbol{\Lambda}\right], \tag{5}$$

$$C = \frac{1}{2\rho T^2} \left\{ (P^{CS} - \rho T)\boldsymbol{\nabla} \cdot \mathbf{u} + \boldsymbol{\Lambda} : \nabla\mathbf{u} + a\rho^2 \boldsymbol{\nabla} \cdot \mathbf{u} \right.$$
$$- K\left[\frac{1}{2}\boldsymbol{\nabla}\rho \cdot \boldsymbol{\nabla}\rho\boldsymbol{\nabla} \cdot \mathbf{u} + \rho\boldsymbol{\nabla}\rho \cdot \boldsymbol{\nabla}(\boldsymbol{\nabla} \cdot \mathbf{u})\right.$$
$$\left.\left. + \boldsymbol{\nabla}\rho \cdot \boldsymbol{\nabla}\mathbf{u} \cdot \boldsymbol{\nabla}\rho\right]\right\}, \tag{6}$$

$$C_q = \frac{1}{\rho T^2} \boldsymbol{\nabla} \cdot (q\rho T\boldsymbol{\nabla} T). \tag{7}$$

Here, ρ, $\mathbf{u}$, and T are the local density, the velocity, and the temperature, respectively. $\boldsymbol{\Lambda} = K\boldsymbol{\nabla}\rho\boldsymbol{\nabla}\rho - K(\rho\nabla^2\rho + |\boldsymbol{\nabla}\rho|^2/2)\mathbf{I} - [\rho T\boldsymbol{\nabla}\rho \cdot \boldsymbol{\nabla}(K/T)]\mathbf{I}$ is the contribution of the density gradient to the pressure tensor, $\mathbf{I}$ is a unit tensor, and K is the surface tension coefficient. P^{CS} indicates the Carnahan-Starling equation of state,

$$P^{CS} = \rho T \frac{1 + \eta + \eta^2 - \eta^3}{(1 - \eta)^3} - a\rho^2, \tag{8}$$

where $\eta = b\rho/4$ and a and b are the attraction and repulsion parameters, respectively. It should be pointed out that the Prandtl number $\text{Pr} = c_p\mu/\kappa_T = \tau/(\tau - q)$ can be adjusted by modulating the parameter q in the term C_q. Here, $\mu = \rho T\tau$, $\kappa_T = c_p\rho T(\tau - q)$, and c_p are the viscosity coefficient, the heat conductivity, and the isobaric heat capacity, respectively.

Under the constraint of $\int f^{eq}\boldsymbol{\Psi}(\mathbf{v})d\mathbf{v} = \sum_l f_l^{eq}\boldsymbol{\Psi}(\mathbf{v}_l)$, Eq. (2) can be discretized in the velocity space by an appropriate discrete velocity model (DVM). Here, the D2V33 model [69] is used. The discrete GLS-Boltzmann equation is written as

$$\frac{\partial f_{ki}}{\partial t} + \mathbf{v}_{ki} \cdot \frac{\partial f_{ki}}{\partial \mathbf{r}} = -\frac{1}{\tau}(f_{ki} - f_{ki}^{eq}) + I_{ki}, \tag{9}$$

where f_{ki}^{eq} (see the Appendix) is the discrete version of the local equilibrium distribution function; I_{ki} takes the following form:

$$I_{ki} = -[A + \mathbf{B} \cdot (\mathbf{v}_{ki} - \mathbf{u}) + (C + C_q)(\mathbf{v}_{ki} - \mathbf{u})^2]f_{ki}^{eq}. \tag{10}$$

Taking the moments of Eq. (9) with the collision invariant vector 1, $\mathbf{v}_{ki}$, and $v_{ki}^2/2$, the generalized Navier-Stokes equations for nonideal fluid with the surface tension effect are obtained [62]:

$$\frac{\partial \rho}{\partial t} + \boldsymbol{\nabla} \cdot (\rho\mathbf{u}) = 0, \tag{11}$$

$$\frac{\partial(\rho\mathbf{u})}{\partial t} + \boldsymbol{\nabla} \cdot (\rho\mathbf{uu} + P^{CS}\mathbf{I}) + \boldsymbol{\nabla} \cdot (\boldsymbol{\Lambda} + \boldsymbol{\Delta}_2^*) = 0, \tag{12}$$

$$\frac{\partial e_T}{\partial t} + \boldsymbol{\nabla} \cdot (e_T\mathbf{u} + P^{CS}\mathbf{u}) + \boldsymbol{\nabla} \cdot \left[(\boldsymbol{\Lambda} + \boldsymbol{\Delta}_2^*) \cdot \mathbf{u}\right.$$
$$\left. + \boldsymbol{\Delta}_{3,1}^* + 2\rho Tq\boldsymbol{\nabla} T\right] = 0, \tag{13}$$

where $\boldsymbol{\nabla} \cdot \boldsymbol{\Lambda}$ is the surface tension [66] and $e_T = \rho T - a\rho^2 + K|\boldsymbol{\nabla}\rho|^2/2 + \rho u^2/2$ is the total energy density.

More importantly, the DBM can quantitatively provide the local TNE effects by defining thermodynamic nonequilibrium moments $\boldsymbol{\Delta}_{m,n}^*$ as

$$\boldsymbol{\Delta}_{m,n}^* = \mathbf{M}_{m,n}^* - \mathbf{M}_{m,n}^{*eq} \tag{14}$$

and

$$\mathbf{M}_{m,n}^*(f_{ki})$$
$$= \sum_{ki} f_{ki} \overbrace{\underbrace{(\mathbf{v}_{ki} - \mathbf{u})(\mathbf{v}_{ki} - \mathbf{u}) \cdots (\mathbf{v}_{ki} - \mathbf{u})}_{n}}^{m} |(\mathbf{v}_{ki} - \mathbf{u})|^{(m-n)}, \tag{15}$$

$$\mathbf{M}_{m,n}^{*eq}(f_{ki}^{eq})$$
$$= \sum_{ki} f_{ki}^{eq} \overbrace{\underbrace{(\mathbf{v}_{ki} - \mathbf{u})(\mathbf{v}_{ki} - \mathbf{u}) \cdots (\mathbf{v}_{ki} - \mathbf{u})}_{n}}^{m} |(\mathbf{v}_{ki} - \mathbf{u})|^{(m-n)}, \tag{16}$$

where m is the number of velocities used in the moment and n is the tensor order. If $m = n$, $\mathbf{M}_{m,n}^* = \mathbf{M}_m^*$. For example,

$$\boldsymbol{\Delta}_2^* = \mathbf{M}_2^* - \mathbf{M}_2^{*eq} = \sum_{ki} (\mathbf{v}_{ki} - \mathbf{u})(\mathbf{v}_{ki} - \mathbf{u})(f_{ki} - f_{ki}^{eq}), \tag{17}$$

$$\boldsymbol{\Delta}_3^* = \mathbf{M}_3^* - \mathbf{M}_3^{*eq}$$
$$= \sum_{ki} (\mathbf{v}_{ki} - \mathbf{u})(\mathbf{v}_{ki} - \mathbf{u})(\mathbf{v}_{ki} - \mathbf{u})(f_{ki} - f_{ki}^{eq}), \tag{18}$$

$$\boldsymbol{\Delta}_{3,1}^* = \mathbf{M}_{3,1}^* - \mathbf{M}_{3,1}^{*eq} = \frac{1}{2}\sum_{ki} (\mathbf{v}_{ki} - \mathbf{u})^2(\mathbf{v}_{ki} - \mathbf{u})(f_{ki} - f_{ki}^{eq}), \tag{19}$$
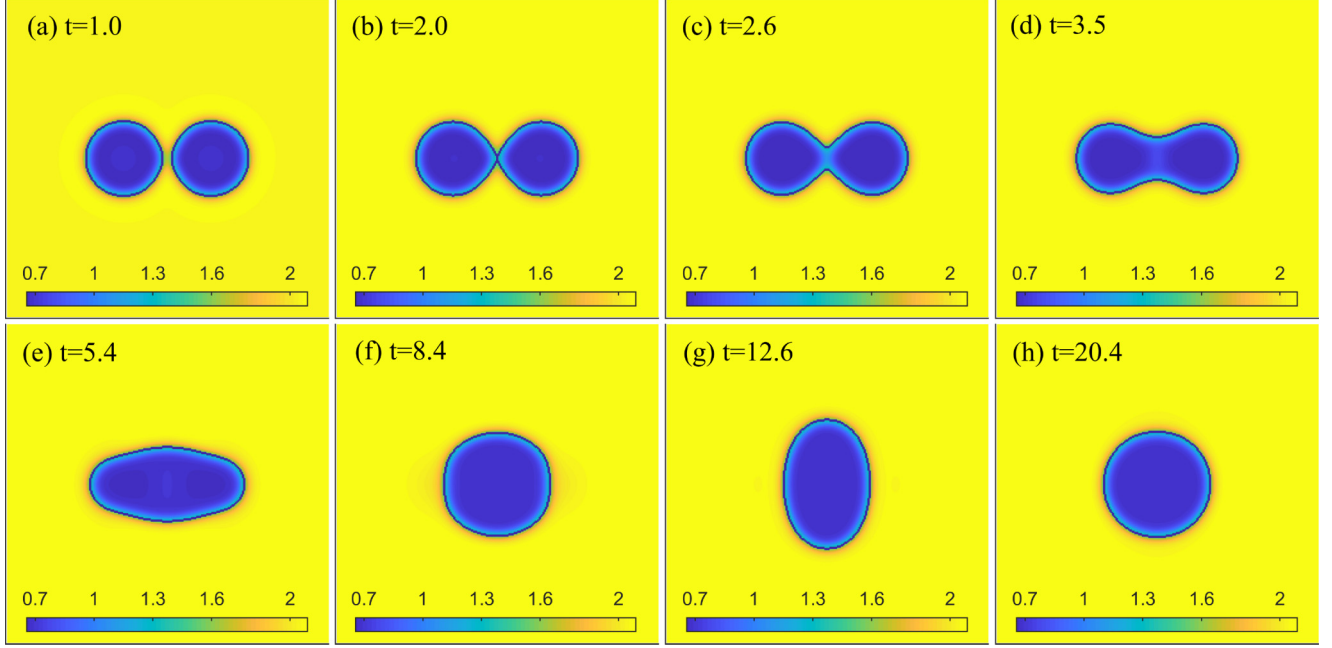
FIG. 1. Maps of density in the process of bubble coalescence at $t = 1.0, 2.0, 2.6, 3.5, 5.4, 8.4, 12.6,$ and 20.4 with $K = 0.00015, \tau = 0.001,$ and Pr $= 0.2$. Here, the grid range of each panel is the whole computational domain $N_x \times N_y = 256 \times 256$, and the color bar at the bottom of each panel refers to fluid density.

$$\boldsymbol{\Delta}^*_{4,2} = \mathbf{M}^*_{4,2} - \mathbf{M}^{*eq}_{4,2}$$

$$= \frac{1}{2} \sum_{ki} (\mathbf{v}_{ki} - \mathbf{u})^2 (\mathbf{v}_{ki} - \mathbf{u})(\mathbf{v}_{ki} - \mathbf{u})\big(f_{ki} - f^{eq}_{ki}\big). \quad (20)$$

$\boldsymbol{\Delta}^*_2$ and $\boldsymbol{\Delta}^*_{3,1}$ are referred to as nonorganized momentum fluxes and nonorganized energy fluxes, respectively. The first-order analytical solutions for those TNE effects are given in Refs. [48,70]:

$$\boldsymbol{\Delta}^{*(1)}_2 = -\rho T \tau [\nabla \mathbf{u} + (\nabla \mathbf{u})^T - \mathbf{I} \nabla \cdot \mathbf{u}], \quad (21)$$

$$\boldsymbol{\Delta}^{*(1)}_{3,1} = -2\rho T \tau \nabla T. \quad (22)$$

It should be pointed out that the external force term is introduced into the model through f^{eq}_{ki} [see Eq. (10)], so the external force term does not introduce additional first-order TNE effects compared with the ideal-gas system but will introduce additional second-order TNE effects [71].

III. SIMULATIONS AND ANALYSIS

In the simulations, all the parameters are nondimensionalized by the actual physical quantities [62]. The actual physical quantities can be recovered from the numerical results if the parameters in the equation of state and the surface tension coefficient of the real fluid can be provided. A fast Fourier transform scheme with 16th order in precision is used to discretize the spatial derivatives; the second-order Runge-Kutta finite difference scheme is utilized to solve the temporal derivative. The computational grids are $N_x \times N_y = 256 \times 256$ with space step $\Delta x = \Delta y = 1/128$; the time step is $\Delta t = 0.0001$. The parameters a and b in the equation of state are chosen to be $a = 2.0$ and $b = 0.4$, fixing the critical point at $T_c = 1.88657, \rho_c = 1.3044,$ and $P_c = 0.8832$.

To numerically study the physical mechanisms of bubble coalescence, the initial state of two stationary bubbles being horizontally abreast is set as

$$\rho(x, y) = \rho_g + \frac{(\rho_l - \rho_g)}{2} \tanh \left[\frac{\sqrt{(x-x_{01})^2 + (y-y_{01})^2} - r_0}{0.5w} \right]$$

$$+ \frac{(\rho_l - \rho_g)}{2} \tanh \left[\frac{\sqrt{(x-x_{02})^2 + (y-y_{02})^2} - r_0}{0.5w} \right]. \quad (23)$$

Here, $\rho_l = 2.0658$ and $\rho_g = 0.6894$ are the densities of the liquid and gas phases with $T = 1.8$; $w = 6.0$ is the width of the boundary layer, $r_0 = 30$ is the radius of the static bubble, (x_{01}, y_{01}) is the center coordinate of the left bubble, and (x_{02}, y_{02}) is the center coordinate of the right bubble. The temperature of the system is free to evolve during the simulations.

A. Nonequilibrium characteristics of bubble coalescence

Two bubbles that are close together will coalesce under the action of the surface tension. Figure 1 shows density patterns at eight characteristic instants with $K = 0.00015, \tau = 0.001,$ and Pr $= 0.2$. Time evolutions of the ratio of minor and major axes L_d $(= L_y/L_x), L_x,$ and L_y are displayed in Figs. 2(a) and 2(b), where L_x and L_y are the major axis and minor axis of the new bubble, respectively. As shown in Fig. 1, the density of the center point of the liquid film between two bubbles is less than the mean density $\rho_{\text{mean}}(t) = [\rho_l(t) + \rho_g(t)]/2$ at $t = 2.0$; then the shape of the coalescing bubble will go through different states: (i) a dumbbell shape at $t = 3.5$, (ii) a fusiform shape at $t = 5.4$, (iii) the first unsteady circle at $t = 8.4$ with $L_d = 1.0$ for the first time [this instant is labeled t_{l1}, as shown in Fig. 2(a)], (iv) a vertical ellipse at $t = 12.6$ (the ratio of minor and major axes is maximum at this time), and (v) an unsteady circle for the second time at $t = 20.4$ with $L_d = 1.0$ again. From Fig. 2(b), it can be found that the first
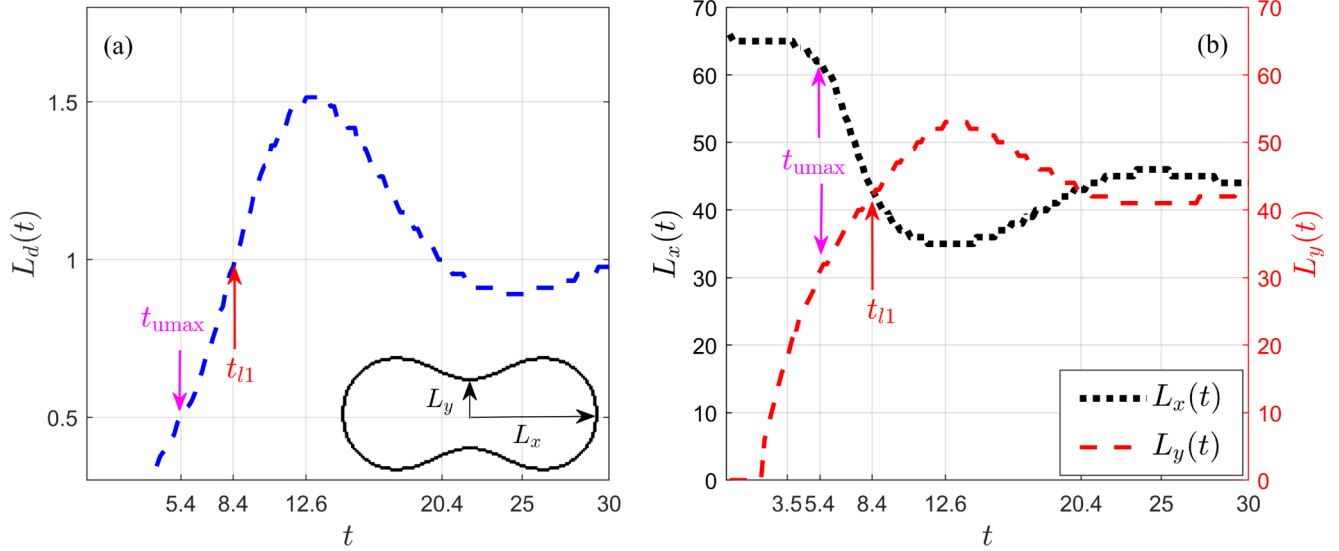
FIG. 2. Temporal evolutions of (a) the ratio of minor and major axes $L_d = L_y/L_x$ and (b) the major axis L_x and the minor axis L_y for $K = 0.00015$, $\tau = 0.001$, and $\text{Pr} = 0.2$.

coalescence phase ($t < t_{l1}$) can be divided into two substages: (i) the fast growing stage of L_y, but L_x remains almost unchanged ($t \leqslant 5.4$), and (ii) the rapidly decreasing stage of L_x ($5.4 < t < 8.4$). Note that when $t = 5.4$, $L_d = 1/2$, and the average coalescence velocity reaches the maximum, which is displayed in Fig. 6 by a blue dashed line. We denote this instant as t_{umax}.

Although the coalescence regime and the damped oscillation in the bubble coalescence process have been extensively studied using diverse experimental, theoretical, and numerical simulation methods from different perspectives [12,14,16–18,32,33,38–40], there are also a lot of valuable physical problems which deserve attention during the first coalescence phase ($t < t_{l1}$). For example, various kinds of nonequilibrium effects are generated and enhanced during this stage.

After the instant of contact ($t = 2.0$), an interface with negative curvature is formed at the saddle point, together with a low temperature and pressure region near the middle liquid film, which can drive mass flux from each bubble to the middle bridge. Therefore, the NOMFs or other nonequilibrium behavior related to mass flux must be relatively strong in the bubble. Equation (21) indicates that $\Delta_{2\alpha\beta}^*$ are all mainly determined by the spatial distribution of the velocity gradient computed assuming a constant value of the viscosity coefficient. As shown in Figs. 3(a) and 3(b), when the two bubbles are close to each other, the intermediate liquid film is thinning. The strong nonequilibrium effects first occur in the liquid film between the two bubbles because of the formation of a local relatively high velocity gradient. As displayed by the black solid line and blue dashed line in Fig. 4, the velocity gradient exhibits a higher value in the lattice nodes indexed from 119 to 137 along the x direction when $t \leqslant 2.6$. Moreover, four small vortices appear on both sides of the central axis under the combined influence of the pressure, the surface tension, and the viscosity [see Figs. 5(a)–5(c)]. Thus, the spatial distribution of Δ_{2xx}^* is positive in the middle and negative on

both sides; the distribution of Δ_{2yy}^* is just the opposite; the spatial distribution of Δ_{2xy}^* is an antisymmetric internal and external double quadrupole structure, and the outside one is dominant. The maximum of Δ_{2xx}^* is reached soon after the merging of the two bubbles ($t = 2.6$) because the surface energy rapidly translates into kinetic energy [14], which results in the largest velocity gradient being formed near the coalescence point, as shown in Fig. 4(b) by the blue dashed line. When $2.6 < t \leqslant 5.4$, the part inside the bubble is gradually mobilized, and the average velocity increases gradually, which can be illustrated by progressively wider profiles of u_x and $\partial u_x/\partial x$ [see the purple dotted lines in Figs. 4(a) and 4(b)]. Hence, the area where $\mathbf{\Delta}_2^*$ dominates progressively increases, and the mean intensity of $\mathbf{\Delta}_2^*$ decreases simultaneously. When $5.4 < t < 8.4$, L_x rapidly decreases [see the black dotted line in Fig. 2(b)], causing the peak of the velocity to step to the outside of the bubble [see Figs. 5(e) and 5(f)], and then Δ_{2xx}^* in the bubble gradually becomes completely positive due to the negative velocity gradient. Δ_{2yy}^* has similar evolvement rules. For Δ_{2xy}^*, when $t \leqslant 5.4$, the relative intensity and major area of the internal quadrupole structure slowly become large by the gradual increasing of the average speed and area of vortex flow [see the middle column in Figs. 3(a)–3(c)]. The internal quadrupole structure also moves to the outside of the bubble, which leads to the formation of an outer octupole structure [see the middle column in Fig. 3(d)] because the centers of the vortex move from the saddle position to outside the bubble [see Figs. 5(b)–5(e)]. When $t \geqslant t_{l1} = 8.4$, the bubble coalescence enters the damping oscillation stage, and the spatial distribution of the three components of $\mathbf{\Delta}_2^*$ will change with the periodic variation of the vortex velocity. For example, the value of L_d is 1.0 at both $t = 8.4$ and $t = 20.4$ [see Fig. 2(a)], but the polarity of $\Delta_{2\alpha\beta}^*$ is the opposite [see Figs. 3(e) and 3(g)], and $t = 12.6$ is the transitional moment of alternation of two polarities. To further study the relationships between TNE and the morphological and kinetics characteristics of bubble coalescence, the statistical averages of four quantities
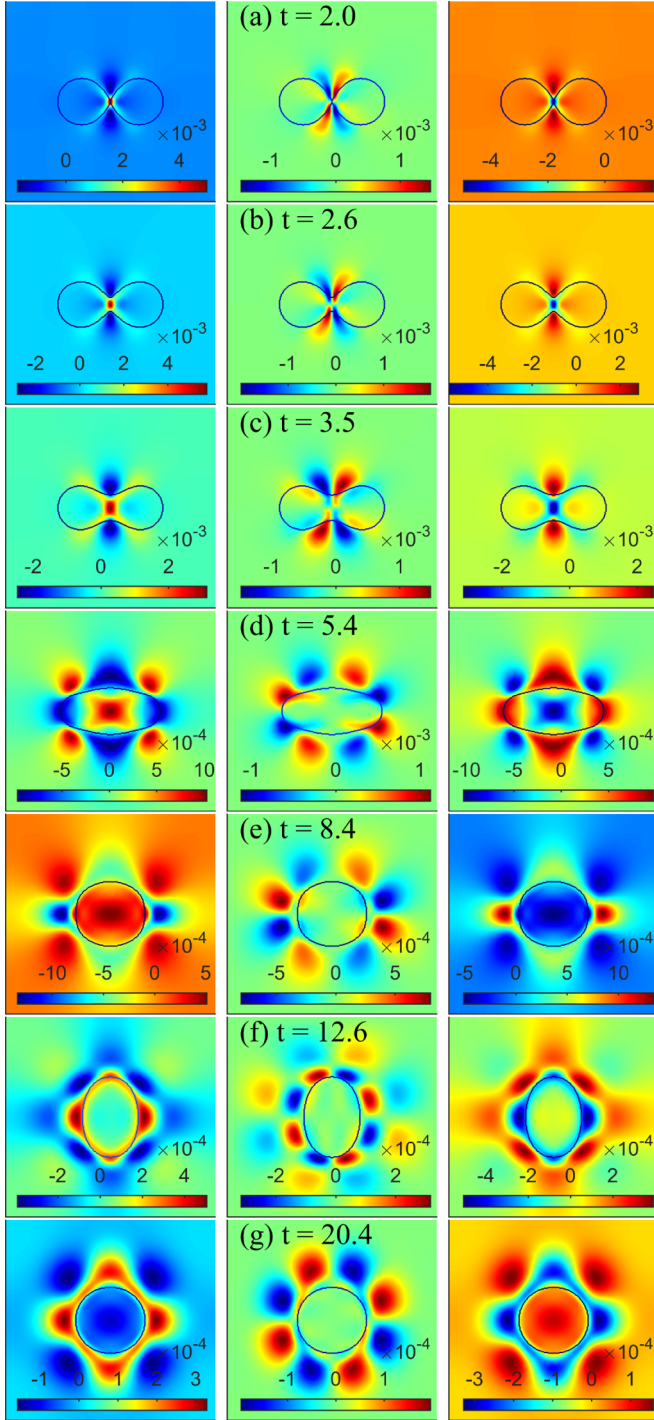
FIG. 3. The spatial distributions of Δ^*_{2xx} (first column), Δ^*_{2xy} (second column), and Δ^*_{2yy} (third column), as captured at the same characteristic times (except for $t = 1.0$) as in Fig. 1, with $K = 0.00015$, $\tau = 0.001$, and $Pr = 0.2$. Here, the grid range of each submap is the whole computational domain $N_x \times N_y = 256 \times 256$, and the color bar at the bottom of each panel refers to the magnitude of $\Delta^*_{2\alpha\beta}$.

are defined as follows:

$$\bar{\Delta}^*_{2\alpha\beta}(t) = \frac{\sum \rho(x, y, t)\Delta^*_{2\alpha\beta}(x, y, t)}{\sum \rho(x, y, t)}, \quad (24)$$
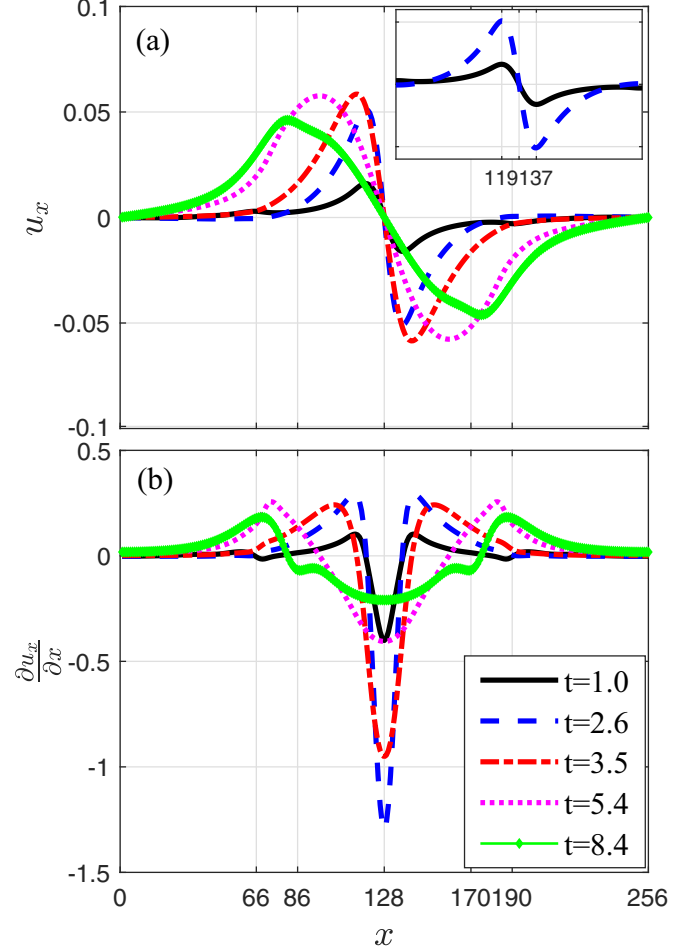
FIG. 4. Distributions of u_x and $\partial u_x/\partial x$ on the horizontal central axis ($y = 128$) at $t = 1.0, 2.6, 3.5, 5.4,$ and 8.4 with $K = 0.00015$, $\tau = 0.001$, and $Pr = 0.2$. Here, $x = 66, 86, 170,$ and 190 are the left and right coordinates of the gas-liquid boundary at $t = 5.4$ and $t = 8.4$, respectively.

$$\bar{u}(t) = \frac{\sum \rho(x, y, t)u_x(x, y, t)}{\sum \rho(x, y, t)}, \quad (25)$$

$$\bar{D}^*(t) = \frac{\sum \rho(x, y, t)\sqrt{\mathbf{\Delta}^{*2}_2 + \mathbf{\Delta}^{*2}_3 + \mathbf{\Delta}^{*2}_{3,1} + \mathbf{\Delta}^{*2}_{4,2}}}{\sum \rho(x, y, t)}, \quad (26)$$

$$\overline{(\nabla\mathbf{u} : \nabla\mathbf{u})^{0.5}}(t) = \frac{\sum \rho(x, y, t)(\nabla\mathbf{u} : \nabla\mathbf{u})^{0.5}}{\sum \rho(x, y, t)}. \quad (27)$$

There are two reasons why we use the density-weighted statistical method [36] to highlight the relationships between the TNE effects and the morphological and kinetic characteristics of bubble coalescence. First, the TNE effects mainly locate in the vicinity of the boundary layer in the coalescing bubble system. Second, we are concerned with the nonequilibrium effects within the bubble, where the density and also the density gradient adjacent to the inner boundary layer are larger than those away from the inner boundary layer. The statistical areas are all in the left half of the computational domain. Equation (24) is the average of $\Delta^*_{2\alpha\beta}$. Based on the analysis of Fig. 3, $\Delta^*_{2yy} + \Delta^*_{2xx} = 0$, and $\bar{\Delta}^*_{2xy} = 0$ due to its spatial antisymmetry, so it just remains to analyze the independent
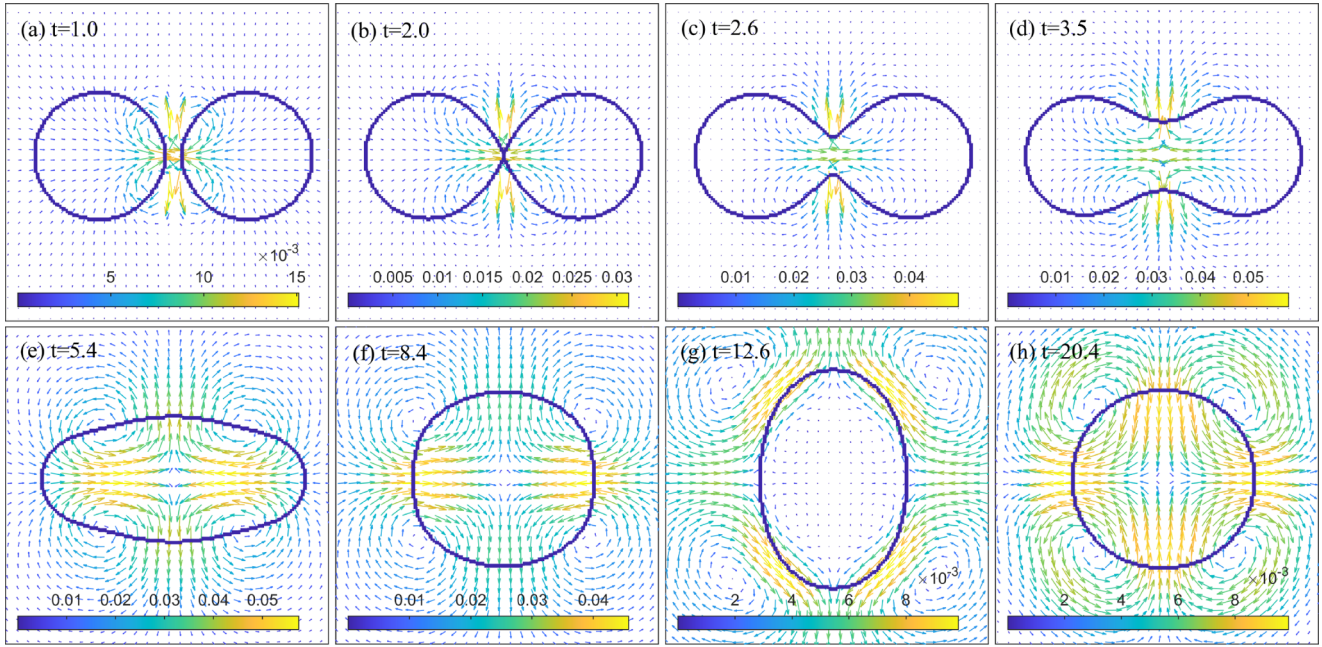
FIG. 5. The velocity vector fields, as captured at the same characteristic times as in Fig. 1, with $K = 0.00015$, $\tau = 0.001$, and Pr $= 0.2$. Here, the grid range of each panel is the partial simulated area $N'_x \times N'_y = 150 \times 150$, with $N'_x = N'_y = 200 - 50$, and the color bar at the bottom of each panel refers to the magnitude of velocity.

one, $\bar{\Delta}^*_{2xx}$. Equations (25)–(27) are the average coalescence velocity, the mean total TNE strength, and the spatial average of the velocity gradient, respectively.

Figure 6 shows the time evolution of $\bar{\Delta}^*_{2xx}(t)$ and $\bar{u}(t)$ with a black dotted line and a blue dashed line, respectively. The evolution of $\bar{\Delta}^*_{2xx}(t)$ is consistent with the analysis of Fig. 3. $\bar{\Delta}^*_{2xx}$ increases due to the locally rapid growth of Δ^*_{2xx} when $t \leqslant 2.6$, as displayed by the black solid and blue dashed lines in Fig. 7. In the time interval $2.6 < t \leqslant 5.4$, $\bar{\Delta}^*_{2xx}(t)$ decreases because the peaks of Δ^*_{2xx} decrease and the areas where Δ^*_{2xx} dominates increase, which can be understood by comparing the blue dashed and purple dotted lines in Fig. 7. $\bar{\Delta}^*_{2xx}(t)$
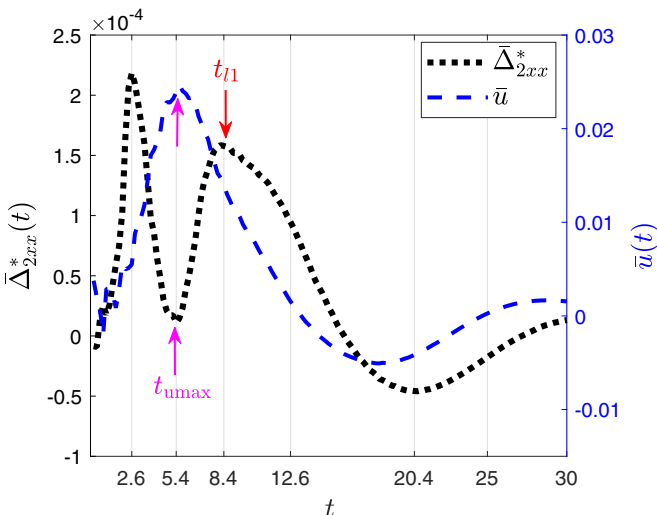
gets the first local minimum at $t = 5.4$; that is, $\bar{\Delta}^*_{2xx}(t)$ gets its first local minimum at $t = t_{\text{umax}}$ because at this instant, the absolute values of the peak values of Δ^*_{2xx} are almost equal and the region where the positive Δ^*_{2xx} dominates is nearly equal to the area where the negative Δ^*_{2xx} dominates. In the period $5.4 < t < 8.4$, $\bar{\Delta}^*_{2xx}(t)$ increases again because
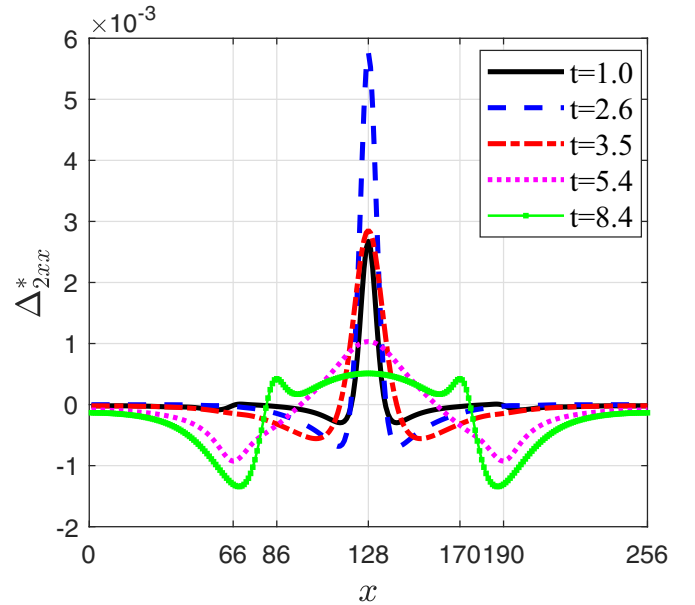

FIG. 7. Distributions of Δ^*_{2xx} on the horizontal central axis ($y = 128$), as captured at the same characteristic times as in Fig. 4, for $K = 0.00015$, $\tau = 0.001$, and Pr $= 0.2$. Here, $x = 66, 86, 170$, and 190 are the left and right coordinates of the gas-liquid boundary at $t = 5.4$ and $t = 8.4$, respectively.

FIG. 6. The temporal profiles of $\bar{\Delta}^*_{2xx}(t)$ and $\bar{u}(t)$ for $K = 0.00015$, $\tau = 0.001$, and Pr $= 0.2$.
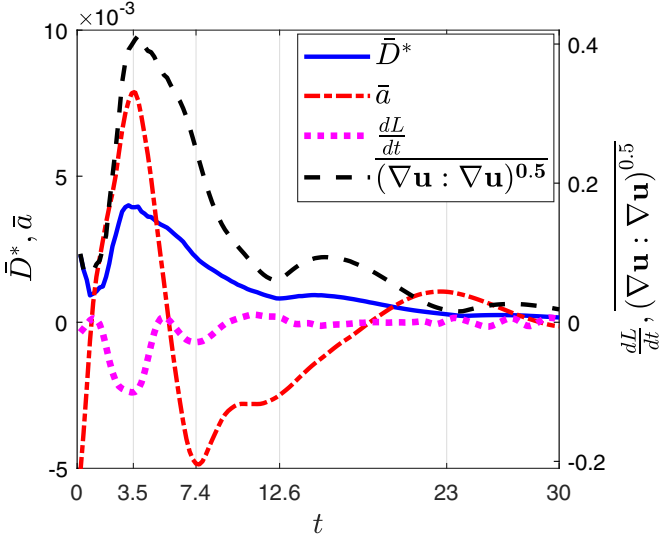
FIG. 8. The temporal profiles of $\bar{D}^*(t)$, the mean acceleration of bubble coalescence $\bar{a}(t) = d\bar{u}/dt$, the slope of boundary length dL/dt, and $\overline{(\nabla \mathbf{u} : \nabla \mathbf{u})^{0.5}}$ for $K = 0.00015$, $\tau = 0.001$, and Pr $= 0.2$.

of Δ_{2xx}^* in the bubble being completely positive, as shown in Fig. 7 by the green line with squares. $\bar{\Delta}_{2xx}^*(t)$ reaches the local
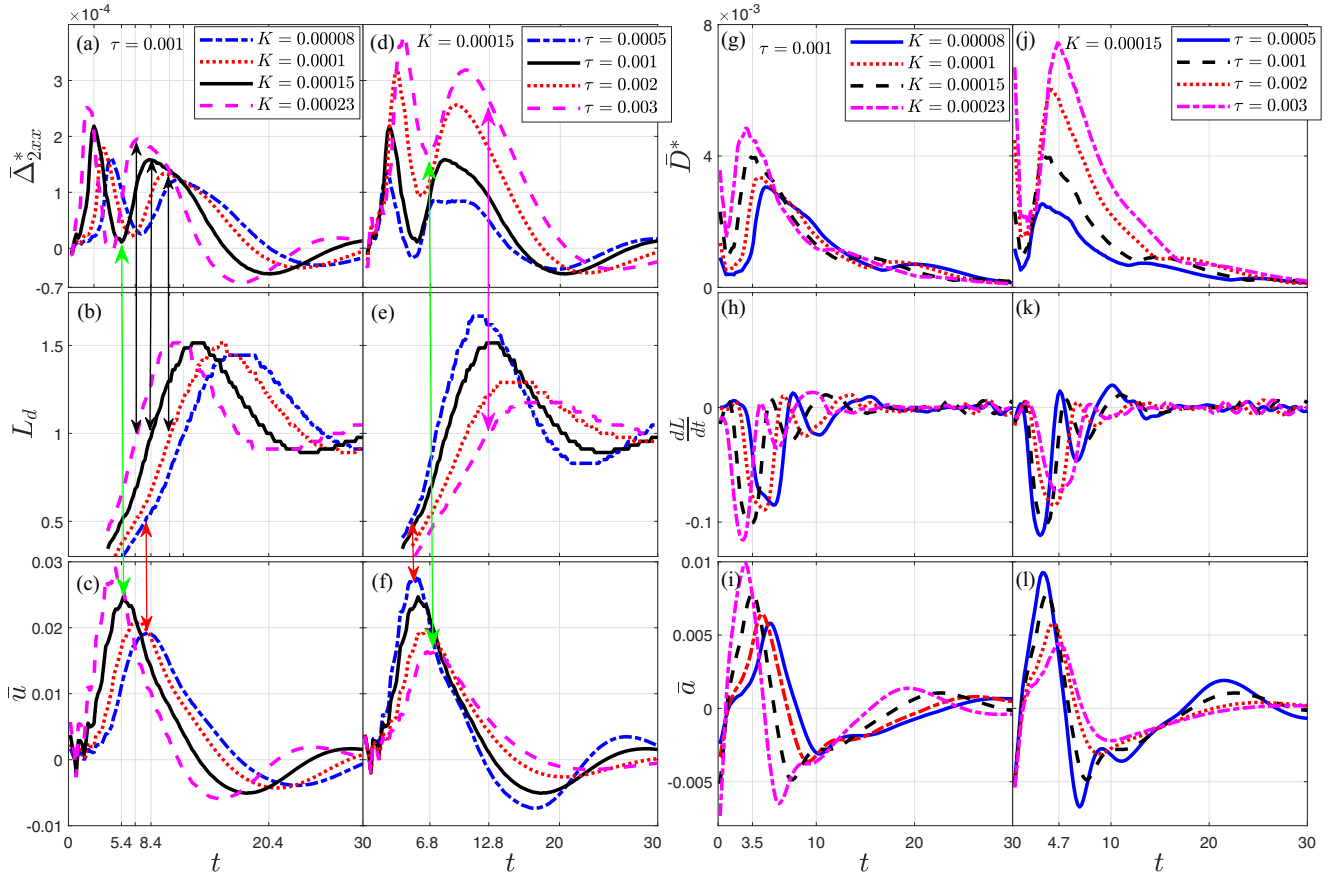
maximum for the second time at $t = t_{l1} = 8.4$; after that, it enters the damping oscillation stage ($t \geqslant t_{l1}$).

The value of $\bar{D}^*(t)$ mainly depends on the strength of $\mathbf{\Delta}_2^*$ and $\mathbf{\Delta}_{4,2}^*$, especially $\mathbf{\Delta}_{4,2}^*$ because its strength is about 5 times $\mathbf{\Delta}_2^*$ [71]. According to the results of Ref. [66], $\overline{(\nabla \mathbf{u} : \nabla \mathbf{u})^{0.5}}$ characterizes the strength of $\mathbf{\Delta}_2^*$ and $\mathbf{\Delta}_{4,2}^*$. Figure 8 demonstrates the evolutions of $\bar{D}^*(t)$ as well as of the mean acceleration $\bar{a}(t) = d\bar{u}/dt$ of bubble coalescence, the slope of boundary length dL/dt, and $\overline{(\nabla \mathbf{u} : \nabla \mathbf{u})^{0.5}}(t)$. It is interesting to find that the trends of $\bar{D}^*(t)$ and $\overline{(\nabla \mathbf{u} : \nabla \mathbf{u})^{0.5}}(t)$ are extraordinarily similar. Moreover, they are strongest at $t = 3.5$; meanwhile, the mean coalescence acceleration is the largest, and the boundary length has the fastest changing rate. As shown in Fig. 2(b), L_x starts to decrease at $t = 3.5$, and the morphology of the new big bubble depends on the evolution of L_x and L_y thereafter, so the boundary length has the largest slope at this instant. This generates the largest energy release rate; thus, $\overline{(\nabla \mathbf{u} : \nabla \mathbf{u})^{0.5}}(t)$ and $\bar{a}(t)$ reach the maximum simultaneously.

B. Effects of surface tension and viscosity

The effects of the coefficient of surface tension and of the viscosity coefficient on bubble coalescence are studied in
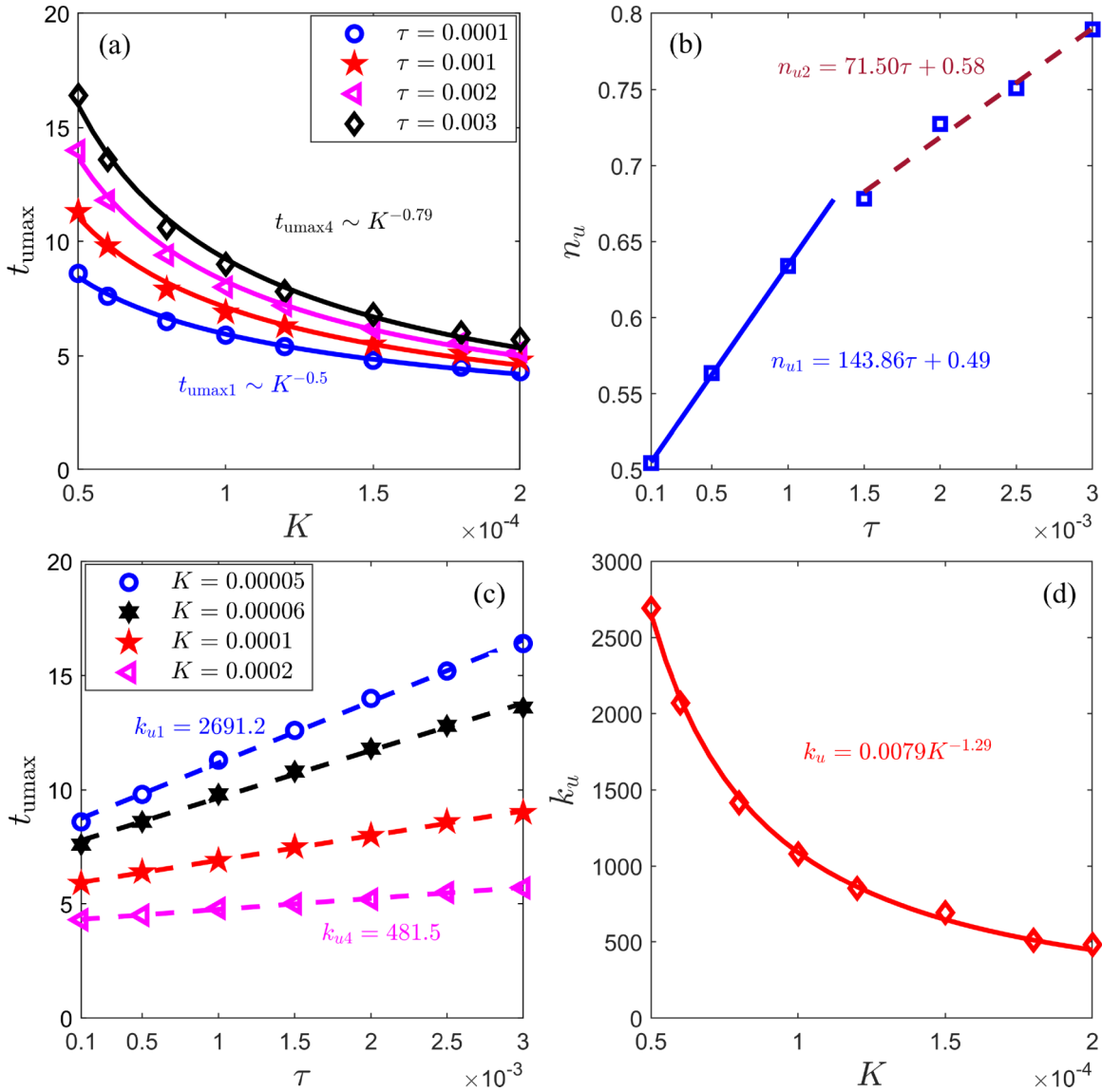

FIG. 9. The influence of the coefficient of surface tension and the viscosity coefficient. (a), (b), and (c) are profiles of $\bar{\Delta}_{2xx}^*(t)$, $L_d = L_y/L_x$, and $\bar{u}(t)$ for $K = 0.0008$, 0.001, 0.0015, and 0.0023 with $\tau = 0.001$. (d), (e), and (f) are profiles of $\tau = 0.0005$, 0.001, 0.002, and 0.003 with $K = 0.00015$. (g), (h), and (i) are profiles of $\bar{D}^*(t)$, dL/dt, and $\bar{a}(t) = d\bar{u}/dt$ with the same parameters as in (a)–(c). (j), (k), and (l) are profiles of $\bar{D}^*(t)$, dL/dt, and $\bar{a}(t)$ with the same parameters as in (d)–(f). Here, the heat conductivity is constant, with $\tau - q = 0.005$.

FIG. 10. Effects of the coefficient of surface tension and the viscosity coefficient on t_{umax}. The relationship between t_{umax} and the coefficient of surface tension K is $t_{umax} \sim K^{-n_u}$, with $n_u = 143.86\tau + 0.49 (\tau < 0.0015)$ and $n_u = 71.50\tau + 0.58 (\tau \geqslant 0.0015)$. Moreover, $n_u \sim 0.5$ for $\tau = 0.0001$, which is consistent with the results of Ref. [14] under the condition of lower viscosity. And there is a linear relationship between t_{umax} and the viscosity coefficient $t_{umax} = k_u\tau + b_u$ with $k_u = 0.0079K^{-1.29}$. Here, $\tau - q = 0.005$ to keep heat conductivity constant.

this section. The viscosity coefficient $\mu = \rho T\tau$ is changed by adjusting the relaxation time τ. Figures 9(a)–9(f) show the evolution curves of $\bar{\Delta}_{2xx}^*(t)$, L_d, and $\bar{u}(t)$; Figs. 9(g)–9(l) show the evolution profiles of $\bar{D}^*(t)$, dL/dt, and $\bar{a}(t)$, respectively. As indicated by the green double arrows, in all cases it is clear that $\bar{\Delta}_{2xx}^*(t)$ reaches its first local minimum at time $t = t_{umax}$, when the average coalescence speed reaches its maximum. As shown by the black double arrows, $\bar{\Delta}_{2xx}^*(t)$ reaches its second local maximum at $t = t_{l1}$, when the ratio between the minor and major bubble axes is $L_d = 1$ for the first time. In particular, when the surface tension is relatively small or when the viscosity is relatively high, $\bar{\Delta}_{2xx}^*(t)$ reaches its second local maximum earlier (i.e., at time $t < t_{l1}$), as shown by the purple double arrow. This happens because in these cases, the viscosity, rather than the surface tension, dominates the evolution of the system, which results in the relatively quick damping of nonequilibrium strength and the slower coalescence process.

Comprehensive statistics demonstrate that the instant when $\bar{\Delta}_{2xx}^*(t)$ reaches its second local maximum is always equal to t_{l1} when Oh $\leqslant 0.17$. Here, the Ohnesorge number Oh $= \mu/\sqrt{\rho_l r_0 \sigma}$ [13] is used to characterize bubble coalescence with $\mu = \rho_l T\tau$, ρ_l, r_0, and $\sigma = K \int_{-\infty}^{+\infty} (\partial\rho/\partial r_\alpha)^2 dr_\alpha$ [72] being the viscosity coefficient, the liquid density, the initial bubble radius, and the surface tension, respectively. In addition, for all L_d, they are about $1/2$ at $t = t_{umax}$, as illustrated by the red double arrows.

There are three main mechanisms (the surface tension, the viscosity, and the inertial force) influencing the process of bubble coalescence, and they dominate at different time periods [12,14]. As a whole, the surface tension is the original driving force of bubble coalescence and determines the initial velocity of the saddle point, so t_{umax} decays in the form of a power law with the increase of the surface tension coefficient K, $t_{umax} \sim K^{-n_u}$ [see Fig. 10(a)]; the viscosity impedes the
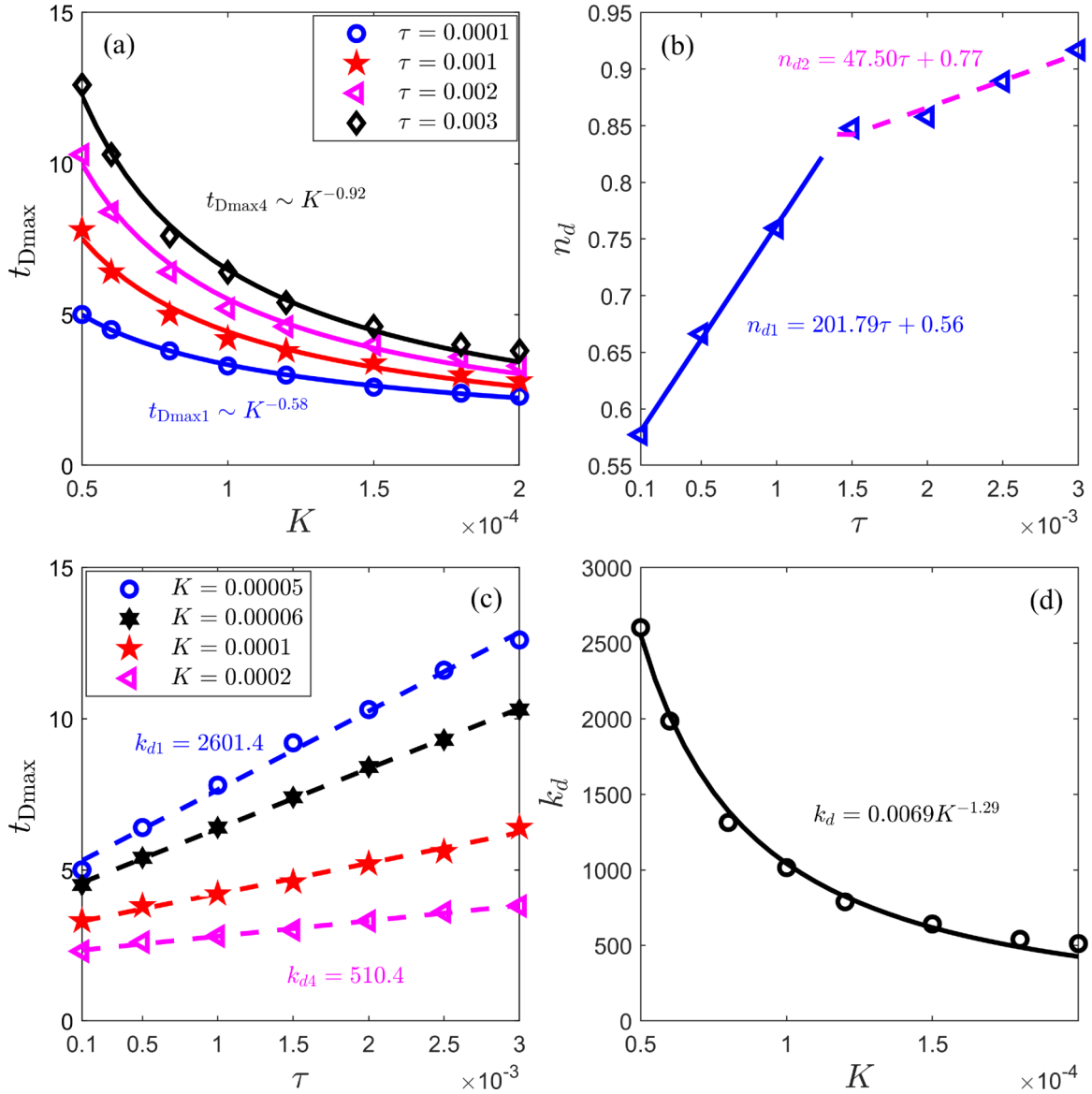
FIG. 11. The effects of the coefficient of surface tension and the viscosity coefficient on t_{Dmax} with $\tau - q = 0.005$.

coalescence progress, which is why t_{umax} linearly increases with the viscosity coefficient, $t_{\text{umax}} = k_u \tau + b_u$ [see Fig. 10(c)]. As shown in Fig. 10(b), the relationship between n_u and τ is linear with positive slopes $k_{nu1} = 143.86$ ($\tau < 0.0015$) and $k_{nu2} = 71.50$ ($\tau \geqslant 0.0015$). This suggests that the fluid viscosity increases the value of t_{umax}. For a larger value of the fluid viscosity, the value of t_{umax} increases, and the growing prefactor of L_y is diminished [32,40]. This causes a reduction of the growth rate of L_d [see Fig. 9(e)] and the relatively large t_{umax} when the surface tension coefficient is lower [see Fig. 10(a)]. In the case of high viscosity, the hindering effect of the viscosity on the growth of L_y becomes stronger; as a result, $k_{nu1} > k_{nu2}$. As exhibited in Fig. 10(d), there is a power-law fitting for the slope $k_u = 0.0079K^{-1.29}$. It is quite clear that the surface tension reduces the effect of the viscosity because the higher the surface tension is, the smaller Oh is, and the larger the growing prefactor of L_y is [32,33,40]. As shown by Figs. 9(g)–9(l), the mean total TNE strength, the average coalescence acceleration, and the absolute value of

the changing rate of the boundary length reach their maxima at the same time in all cases. The effects of the coefficient of surface tension and of the viscosity coefficient on t_{Dmax}, which is the instant when $\bar{D}^*(t)$ reaches the maximum, are shown in Fig. 11. On the basis of Figs. 11(a) and 11(b), the relation between t_{Dmax} and the surface tension coefficient K also presents a power-law function: $t_{\text{Dmax}} \sim K^{-n_d}$, with $n_d = 201.79\tau + 0.56(\tau < 0.0015)$ and $n_d = 47.50\tau + 0.77(\tau \geqslant 0.0015)$. As shown in Figs. 11(c) and 11(d), there is a linear relation between t_{Dmax} and the viscosity coefficient: $t_{\text{Dmax}} = k_d \tau + b_d$, with $k_d = 0.0069K^{-1.29}$. Here, the variation rules of t_{Dmax} are very similar to those of t_{umax}.

The effects of the coefficient of surface tension and of the viscosity coefficient on $\bar{D}^*_{\text{max}}$, which is the maximum value of $\bar{D}^*(t)$, are displayed in Fig. 12. According to Figs. 12(a) and 12(b), $\bar{D}^*_{\text{max}}$ and K show a linear relationship, $\bar{D}^*_{\text{max}} = k_D K + b_D$, with $k_D = 1386\tau^{0.67}$. From Figs. 12(c) and 12(d), the relation between $\bar{D}^*_{\text{max}}$ and the viscosity coefficient is a power-law function $\bar{D}^*_{\text{max}} \sim \tau^h$, with $h = 372K + 0.53$.
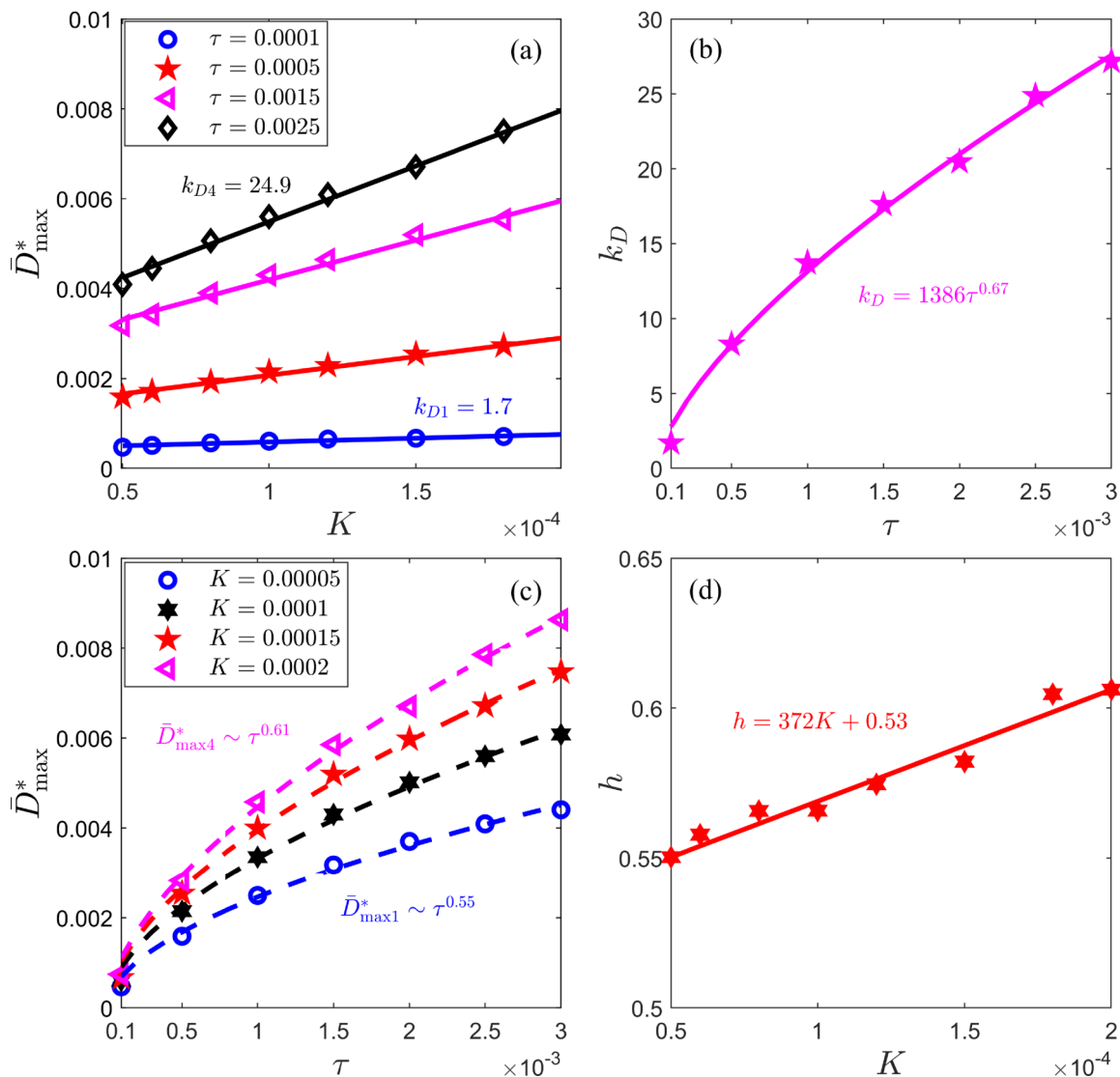
FIG. 12. The effects of the coefficient of surface tension and the viscosity coefficient on $\bar{D}^*_{\max}$ with $\tau - q = 0.005$.
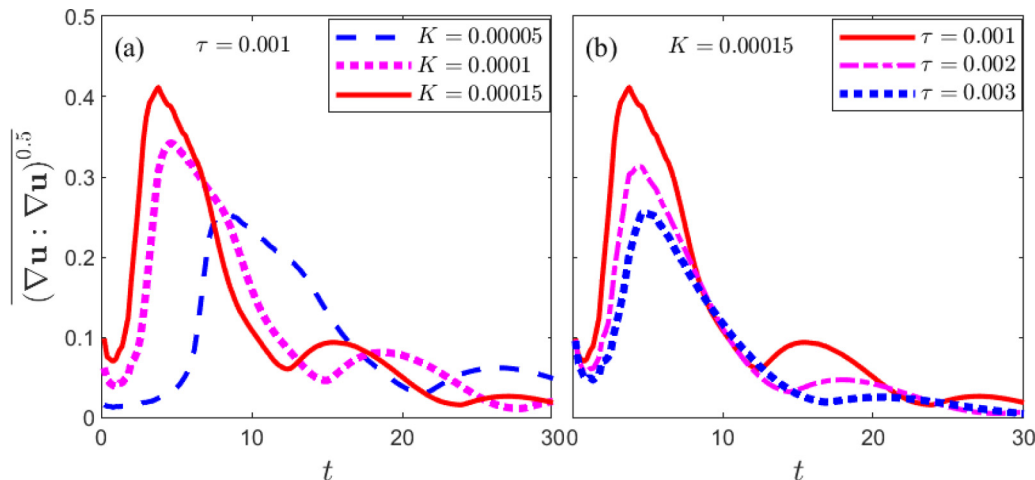

FIG. 13. The effects of the coefficient of surface tension and the viscosity coefficient on $\overline{(\nabla \mathbf{u} : \nabla \mathbf{u})^{0.5}}$ with $\tau - q = 0.005$.
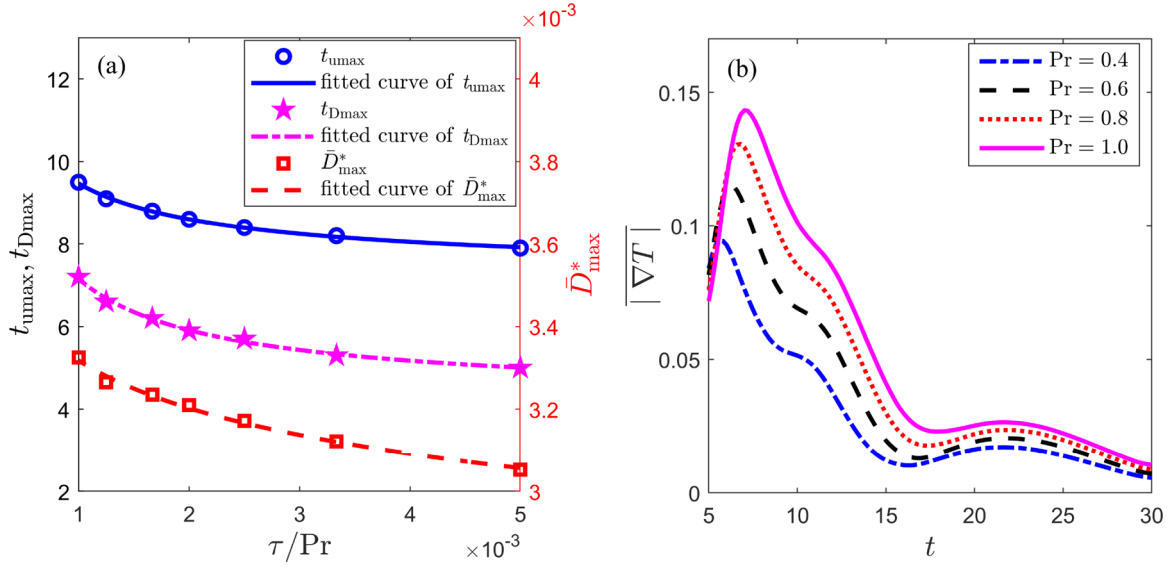
FIG. 14. The effects of heat conductivity and Pr. (a) Effects of heat conductivity on t_{umax}, t_{Dmax}, and $\bar{D}^*_{\text{max}}$. (b) Effect of Pr on the evolution of $\overline{|\nabla T|}$. Here, $K = 0.00008$, $\tau = 0.001$.

Obviously, the surface tension and the viscosity both contribute to the growth of $\bar{D}^*_{\text{max}}$ because the surface tension promotes the velocity gradient $\overline{(\nabla\mathbf{u} : \nabla\mathbf{u})^{0.5}}$ [see Fig. 13(a)] and the viscosity is the primary driving force of TNE. As shown in Fig. 13(b), τ has tripled, but the peak value of $\overline{(\nabla\mathbf{u} : \nabla\mathbf{u})^{0.5}}$ decreases only 1.62 times. Although the prefactors of the first order of $\mathbf{\Delta}^*_{m,n}$ are proportional to τ [71], our result is $\bar{D}^*_{\text{max}} \sim \tau^h (0 < h < 1)$ because the model we used essentially considers not only the first order TNE but also the second order TNE, and the second order one is always the reverse of the first order one in a two-phase flow system.

C. Effects of heat conduction

The influence of heat conduction on t_{umax}, t_{Dmax}, and $\bar{D}^*_{\text{max}}$ is given in Fig. 14(a). Here, the heat conductivity is
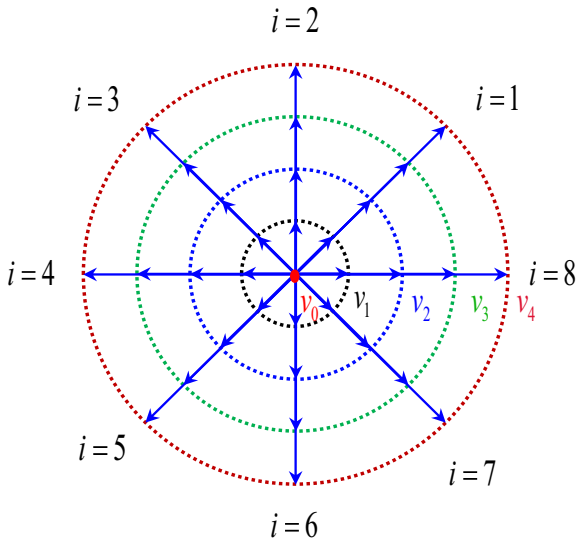
changed by adjusting Pr with fixed $\tau = 0.001$. It can be found that t_{umax}, t_{Dmax}, and $\bar{D}^*_{\text{max}}$ all decrease with τ/Pr. The relations between t_{umax}, t_{Dmax}, and $\bar{D}^*_{\text{max}}$ and τ/Pr are $t_{\text{umax}} = 0.024(\tau/\text{Pr})^{-0.66} + 7.1$, $t_{\text{Dmax}} = 0.017(\tau/\text{Pr})^{-0.75} + 4.1$, and $\bar{D}^*_{\text{max}} = 0.002(\tau/\text{Pr})^{-0.057} + 0.00035$, respectively. It is obvious that the effect of the heat conduction accelerates bubble coalescence and restrains the growth of TNE. Because the heat flow is enhanced with the increase of the heat conductivity, the temperature distribution in the system is more uniform. The higher Pr is, the lower the heat conductivity is. As shown in Fig. 14(b), the average $\overline{|\nabla T|}$ increases with the enhancement of Pr; thus, the strengths of the TNE effects positively associated with ∇T, such as $\mathbf{\Delta}^*_3$ and $\mathbf{\Delta}^*_{3,1}$, decrease with the increase of τ/Pr. Here, $\overline{|\nabla T|} = \sum \rho(x, y, t)\sqrt{(\partial T/\partial x)^2 + (\partial T/\partial y)^2} / \sum \rho(x, y, t)$.

IV. CONCLUSIONS

In this paper, we have studied the thermodynamic nonequilibrium effects during the coalescence of two initially motionless bubbles using a two-dimensional discrete Boltzmann model. Our study focused on two aspects: (i) the relations between the thermodynamic nonequilibrium behaviors inside the bubble system and the characteristic quantities describing the morphology and kinematic features of bubble coalescence before the formation of the first unsteady circular and (ii) the influence of the surface tension, the viscosity, and the heat conduction on (a) the average value of the *xx* component of nonorganized momentum flux, i.e., $\bar{\Delta}^*_{2xx}$, (b) the characteristic time t_{umax} when the average coalescence speed reaches its maximum, (c) the characteristic time t_{Dmax} when the average total thermodynamic nonequilibrium strength becomes the strongest, and (d) the peak value of the average thermodynamic nonequilibrium strength $\bar{D}^*_{\text{max}}$.

The dynamical and complex spatial distributions of $\Delta^*_{2\alpha\beta}$ during bubble coalescence were investigated in detail. The strong nonequilibrium effects first occur in the middle of

FIG. 15. Schematic diagram of the discrete velocity model.

two bubbles. Thereafter, the thermodynamic nonequilibrium strengths increase rapidly in this local region and reach the maximum soon after the merging of the two bubbles. After that, the dominating regions of $\Delta^*_{2\alpha\beta}$ gradually become larger. Δ^*_{2xx} and Δ^*_{2yy} have antisymmetrical spatial distributions. The distribution of Δ^*_{2xy} changes from an antisymmetric internal and external double quadrupole structure to an outer octupole structure. Their polarities change with the variation of the vortical direction of the velocity field periodically.

The mean value of Δ^*_{2xx} in the bubble, $\bar{\Delta}^*_{2xx}$, which integrates kinematic, morphological, and nonequilibrium features, can be used to calibrate the three stages of bubble coalescence. In the first stage (before $\bar{\Delta}^*_{2xx}$ reaches its first local minimum), the minor axis (the neck radius) grows apace until the ratio of minor and major axes is 1/2 and the average coalescence speed gradually increases to the maximum. In the second stage (before $\bar{\Delta}^*_{2xx}$ reaches its second local maximum), the decreasing rate of the major axis exceeds the increasing rate of the minor axis until the ratio of minor and major axes is 1. In the third stage, the system enters the damping oscillation stage. Due to the major axis starting to decrease, the absolute value of the slope of the boundary length reaches the maximum at this time, which leads to the fastest release of surface energy. Thus, both the average total TNE strength in the bubble and the mean acceleration of bubble coalescence reach the maximum simultaneously.

As mentioned in Refs. [12,14,32,33], the surface tension enhances the growth of the minor axis, while the viscosity inhibits it. The relations between the physical quantities that we care about (t_{umax}, t_{Dmax}, and $\bar{D}^*_{max}$) and the surface tension coefficient and the viscosity coefficient were revealed in detail. The heat conduction accelerates the bubble coalescence and restrains the growth of the thermodynamic nonequilibrium effects. This agrees with the results of Refs. [62,63] that the heat conduction facilitates the merging of small domains in the stage of domain growth. In addition, for any parameter we focused on, the ratio of minor and major axes is always about 1/2 when their average coalescence speeds reach the maxima.

The thermodynamic nonequilibrium effects present some insights into coalescence behavior. At the same time, the current study presents a way to detect the progress of bubble coalescence in engineering applications.

APPENDIX

The D2V33 [69] model reads

$$\mathbf{v}_0 = 0, \mathbf{v}_{ki} = v_k\left[\cos\left(\frac{i}{4}\pi\right), \sin\left(\frac{i}{4}\pi\right)\right], \tag{A1}$$

where $k = 1, 2, 3, 4$ indicates the kth group of particle velocities whose speed is v_k and $i = 1, \ldots, 8$ is the direction of v_k, as shown in Fig. 15. We stress that the DVM is selected according to modeling accuracy and stability of the model. The discrete equilibrium distribution function f^{eq}_{ki} is [69]

$$f^{eq}_{ki} = \rho F_k\left[\left(1 - \frac{u^2}{2T} + \frac{u^4}{8T^2}\right) + \frac{\mathbf{v}_{ki}\cdot\mathbf{u}}{T}\left(1 - \frac{u^2}{2T}\right) + \frac{(\mathbf{v}_{ki}\cdot\mathbf{u})^2}{2T^2}\left(1 - \frac{u^2}{2T}\right) + \frac{(\mathbf{v}_{ki}\cdot\mathbf{u})^3}{6T^3} + \frac{(\mathbf{v}_{ki}\cdot\mathbf{u})^4}{24T^4}\right], \tag{A2}$$

with

$$F_1 = \frac{48T^4 - 6(v_2^2 + v_3^2 + v_4^2)T^3 + (v_2^2v_3^2 + v_2^2v_4^2 + v_3^2v_4^2)T^2 - \frac{1}{4}v_2^2v_3^2v_4^2T}{v_1^2(v_1^2 - v_2^2)(v_1^2 - v_3^2)(v_1^2 - v_4^2)}, \tag{A3}$$

$$F_2 = \frac{48T^4 - 6(v_1^2 + v_3^2 + v_4^2)T^3 + (v_1^2v_3^2 + v_1^2v_4^2 + v_3^2v_4^2)T^2 - \frac{1}{4}v_1^2v_3^2v_4^2T}{v_2^2(v_2^2 - v_1^2)(v_2^2 - v_3^2)(v_2^2 - v_4^2)}, \tag{A4}$$

$$F_3 = \frac{48T^4 - 6(v_1^2 + v_2^2 + v_4^2)T^3 + (v_1^2v_2^2 + v_1^2v_4^2 + v_2^2v_4^2)T^2 - \frac{1}{4}v_1^2v_2^2v_4^2T}{v_3^2(v_3^2 - v_1^2)(v_3^2 - v_2^2)(v_3^2 - v_4^2)}, \tag{A5}$$

$$F_4 = \frac{48T^4 - 6(v_1^2 + v_2^2 + v_3^2)T^3 + (v_1^2v_2^2 + v_1^2v_3^2 + v_2^2v_3^2)T^2 - \frac{1}{4}v_1^2v_2^2v_3^2T}{v_4^2(v_4^2 - v_1^2)(v_4^2 - v_2^2)(v_4^2 - v_3^2)}, \tag{A6}$$

$$F_0 = 1 - 8(F_1 + F_2 + F_3 + F_4). \tag{A7}$$

[1] Z. Zhang, W. Liu, and M. L. Free, J. Electrochem. Soc. **167**, 013532 (2020).

[2] R. Kaur, M. Ramakrishna, and K. D. P. Nigam, Rev. Chem. Eng. **23**, 247 (2007).

[3] C. L. Muhich, B. D. Ehrhart, I. Al-Shankiti, B. J. Ward, C. B. Musgrave, and A. W. Weimer, Wiley Interdiscip. Rev.: Energy Environ. **5**, 261 (2016).

[4] M. K. H. Al-Mashhadani, S. J. Wilkinson, and W. B. Zimmerman, Chem. Eng. Sci. **137**, 243 (2015).

[5] N. Matsuki, S. Ichiba, T. Ishikawa, O. Nagano, M. Takeda, Y. Ujike, and T. Yamaguchi, Eur. Biophys. J. **41**, 571 (2012).

[6] J. W. Alexander, L. Stephan, and M. Sylvio, Biophys. J. **93**, 4268 (2007).

[7] A. Doostmohammadi, S. P. Thampi, T. B. Saw, C. T. Lim, B. Ladoux, and J. M. Yeomans, Soft Matter **11**, 7328 (2015).

[8] G. Xu, Z. Sun, and X. Zhang, Ann. Nucl. Energy **151**, 107905 (2021).

[9] D. Jo and S. T. Revankar, Chem. Eng. Sci. **64**, 3179 (2009).

[10] D. Jo and S. T. Revankar, Chem. Eng. Sci. **65**, 4231 (2010).

[11] J. Eggers, J. R. Lister, and H. A. Stone, J. Fluid Mech. **401**, 293 (1999).

[12] J. D. Paulsen, R. Carmigniani, A. Kannan, J. C. Burton, and S. R. Nagel, Nat. Commun. **5**, 3182 (2014).

[13] S. Zhou, Y. Cao, R. Chen, T. Sun, K. Fezzaa, H. Yu, and L. Zhu, Exp. Therm. Fluid Sci. **98**, 362 (2018).

[14] R. L. Stover, C. W. Tobias, and M. M. Denn, AIChE J. **43**, 2385 (1997).

[15] P. Lv, P. Peñas, H. Le The, J. Eijkel, A. van den Berg, X. Zhang, and D. Lohse, Phys. Rev. Lett. **127**, 235501 (2021).

[16] S. Orvalho, M. C. Ruzicka, G. Olivieri, and A. Marzocchella, Chem. Eng. Sci. **134**, 205 (2015).

[17] S. Orvalho, P. Stanovsky, and M. C. Ruzicka, Chem. Eng. J. **406**, 125926 (2021).

[18] J. D. Paulserr, J. C. Burton, S. R. Nagel, S. Appathurai, M. T. Harris, and O. A. Basaran, Proc. Natl. Acad. Sci. USA **109**, 6857 (2012).

[19] D. Zang, K. Lin, L. Li, Z. Chen, X. Li, and X. Geng, Appl. Phys. Lett. **110**, 121602 (2017).

[20] R. D. Kirkpatrick and M. J. Lockett, Chem. Eng. Sci. **29**, 2363 (1974).

[21] M. J. Prince and H. W. Blanch, AIChE J. **36**, 1485 (1990).

[22] S. Ata, N. Ahmed, and G. J. Jameson, Int. J. Miner. Process. **72**, 255 (2003).

[23] R. Han, A.-M. Zhang, S. Li, and Z. Zong, Phys. Fluids **30**, 042107 (2018).

[24] T. Li, A.-M. Zhang, S.-P. Wang, G.-Q. Chen, and S. Li, Phys. Fluids **31**, 092108 (2019).

[25] I. U. Vakarelski, R. Manica, X. Tang, S. J. O'Shea, G. W. Stevens, F. Grieser, R. R. Dagastine, and D. Y. C. Chan, Proc. Natl. Acad. Sci. USA **107** 11177 (2010).

[26] D. Y. Chan, E. Klaseboer, and R. Manica, Adv. Colloid Interface Sci. **165**, 70 (2011).

[27] C. Shi, X. Cui, L. Xie, Q. Liu, D. Y. Chan, J. N. Israelachvili, and H. Zeng, ACS Nano **9**, 95 (2015).

[28] Y. Xing, X. Gui, L. Pan, B.-E. Pinchasik, Y. Cao, J. Liu, M. Kappl, and H.-J. Butt, Adv. Colloid Interface Sci. **246**, 105 (2017).

[29] F. Janssen, A. G. Wouters, E. Chatzigiannakis, J. A. Delcour, and J. Vermant, Food Hydrocolloids **116**, 106624 (2021).

[30] B. Liu, R. Manica, Q. Liu, E. Klaseboer, Z. Xu, and G. Xie, Phys. Rev. Lett. **122**, 194501 (2019).

[31] H. S. Alam, P. Sutikno, T. A. Fauzi Soelaiman, and A. T. Sugiarto, Eng. Appl. Comput. Fluid Mech. **16**, 677 (2022).

[32] J. P. Munro, C. R. Anthony, O. A. Basaran, and J. R. Lister, J. Fluid Mech. **773**, R3 (2015).

[33] Á. M. Soto, T. Maddalena, A. Fraters, D. Van Der Meer, and D. Lohse, J. Fluid Mech. **846**, 143 (2018).

[34] T. T. Duignan, J. Colloid Interface Sci. **600**, 338 (2021).

[35] H. W. Zheng, C. Shu, and Y. T. Chew, Phys. Rev. E **72**, 056705 (2005).

[36] H. W. Zheng, C. Shu, and Y. T. Chew, J. Comput. Phys. **218**, 353 (2006).

[37] R. Chen, H. Yu, L. Zhu, R. M. Patil, and T. Lee, AIChE J. **63**, 1441 (2017).

[38] R. Chen, J. Zeng, and H. Yu, Comput. Fluids **183**, 38 (2019).

[39] R. Chen, H. W. Yu, J. Zeng, and L. Zhu, Phys. Rev. E **101**, 023106 (2020).

[40] C. R. Anthony, P. M. Kamat, S. S. Thete, J. P. Munro, J. R. Lister, M. T. Harris, and O. A. Basaran, Phys. Rev. Fluids **2**, 083601 (2017).

[41] R. Chen, S. Zhou, L. Zhu, L. Zhu, W. Yan, and H. Yu, Phys. Fluids **33**, 043320 (2021).

[42] A. J. Wagner, L. Giraud, and C. E. Scott, Comput. Phys. Commun. **129**, 227 (2000).

[43] Z. Chai, J. Lu, B. Shi, and Z. Guo, Int. J. Heat Mass Transfer **54**, 3009 (2011).

[44] Q. Li, K. H. Luo, Q. Kang, Y. He, Q. Chen, and Q. Liu, Prog. Energy Combust. Sci. **52**, 62 (2016).

[45] A. Xu, G. Zhang, Y. Gan, F. Chen, and X. Yu, Front. Phys. **7**, 582 (2012).

[46] A. Xu, C. Lin, G. Zhang, and Y. Li, Phys. Rev. E **91**, 043306 (2015).

[47] A. Xu, G. Zhang, Y. Zhang, and Y. Gan, in *Proceedings of the 31st International Symposium on Rarefied Gas Dynamics, Glasgow, 2018*, edited by Y. Zhang, D. R. Emerson, D. Lockerby, and L. Wu, AIP Conf. Proc. No. 2132 (AIP, Melville, 2019), and Flows: Physics and beyond (unpublished), available at https://mp.weixin.qq.com/s/WwHnZNX42f7taw_zSxZO5g.

[48] Y. Gan, A. Xu, G. Zhang, Y. Zhang, and S. Succi, Phys. Rev. E **97**, 053312 (2018).

[49] Y. Zhang, A. Xu, G. Zhang, Z. Chen, and P. Wang, Comput. Phys. Commun. **238**, 50 (2019).

[50] A. Xu, G. Zhang, and Y. Zhang, in *Kinetic Theory*, edited by G. Z. Kyzas and A. C. Mitropoulos (InTech, Rijeka, Croatia, 2018), Chap. 2.

[51] F. Chen, A. Xu, and G. Zhang, Phys. Fluids **30**, 102105 (2018).

[52] A. Xu, J. Song, F. Chen, K. Xie, and Y. Ying, Chin. J. Comput. Phys. **38**, 631 (2021).

[53] F. Chen, A. Xu, and G. Zhang, Front. Phys. **11**, 114703 (2016).

[54] Y. Gan, A. Xu, G. Zhang, C. Lin, and Z. Liu, Front. Phys. **14**, 43602 (2019).

[55] H. Lai, A. Xu, G. Zhang, Y. Gan, Y. Ying, and S. Succi, Phys. Rev. E **94**, 023106 (2016).

[56] C. Lin, A. Xu, G. Zhang, K. H. Luo, and Y. Li, Phys. Rev. E **96**, 053305 (2017).

[57] H. Ye, H. Lai, D. Li, Y. Gan, C. Lin, L. Chen, and A. Xu, Entropy **22**, 500 (2020).

[58] C. Lin, A. Xu, G. Zhang, and Y. Li, Combust. Flame **164**, 137 (2016).

[59] Y. Zhang, A. Xu, G. Zhang, C. Zhu, and C. Lin, Combust. Flame **173**, 483 (2016).

[60] Y. Zhang, A. Xu, G. Zhang, and Z. Chen, Commun. Theor. Phys. **71**, 117 (2019).

[61] Y. Gan, A. Xu, G. Zhang, and S. Succi, Soft Matter **11**, 5336 (2015).

[62] Y. Zhang, A. Xu, G. Zhang, Y. Gan, Z. Chen, and S. Succi, Soft Matter **15**, 2245 (2019).

[63] Y. Gan, A. Xu, G. Zhang, P. Zhang, and Y. Li, Europhys. Lett. **97**, 44002 (2012).

[64] Y. Gan, A. Xu, G. Zhang, and Y. Li, Front. Phys. **7**, 481 (2012).

[65] Y. Gan, A. Xu, G. Zhang, Y. Li, and H. Li, Phys. Rev. E **84**, 046715 (2011).

[66] Y. Zhang, A. Xu, J. Qiu, H. Wei, and Z. Wei, Front. Phys. **15**, 62503 (2020).

[67] P. L. Bhatnagar, E. P. Gross, and M. Krook, Phys. Rev. **94**, 511 (1954).

[68] G. Gonnella, A. Lamura, and V. Sofonea, Phys. Rev. E **76**, 036703 (2007).

[69] M. Watari and M. Tsutahara, Phys. Rev. E **67**, 036306 (2003).

[70] Y. Gan, A. Xu, G. Zhang, and H. Lai, Proc. IMechE, Part C: J. Mechanical Engineering Science **232**, 477 (2018).

[71] Y. Gan, A. Xu, H. Lai, W. Li, G. Sun, and S. Succi, arXiv:2203.12458.

[72] T. Inamuro, N. Konishi, and F. Ogino, Comput. Phys. Commun. **129**, 32 (2000).